# Photothermal Nanotherapeutics and Nanodiagnostics for Selective Killing of Bacteria Targeted with Gold Nanoparticles

Vladimir P. Zharov,* Kelly E. Mercer,† Elena N. Galitovskaya,* and Mark S. Smeltzer†
*Philips Classic Laser Laboratories, and †Department of Microbiology and Immunology, University of Arkansas for Medical Sciences, Little Rock, Arkansas

ABSTRACT We describe a new method for selective laser killing of bacteria targeted with light-absorbing gold nanoparticles conjugated with specific antibodies. The multifunctional photothermal (PT) microscope/spectrometer provides a real-time assessment of this new therapeutic intervention. In this integrated system, strong laser-induced overheating effects accompanied by the bubble-formation phenomena around clustered gold nanoparticles are the main cause of bacterial damage. PT imaging and time-resolved monitoring of the integrated PT responses assessed these effects. Specifically, we used this technology for selective killing of the Gram-positive bacterium *Staphylococcus aureus* by targeting the bacterial surface using 10-, 20-, and 40-nm gold particles conjugated with anti-protein A antibodies. Labeled bacteria were irradiated with focused laser pulses (420–570 nm, 12 ns, 0.1–5 J/cm$^2$, 100 pulses), and laser-induced bacterial damage observed at different laser fluences and nanoparticle sizes was verified by optical transmission, electron microscopy, and conventional viability testing.

## INTRODUCTION

*Staphylococcus aureus* (*S. aureus*) is a significant human pathogen responsible for a wide range of diseases such as skin and wound infections, toxic shock syndrome, septic arthritis, endocarditis, and osteomyelitis. Increasingly, these infections are caused by bacterial strains resistant to standard antimicrobial treatments (1,2). Some alternative approaches for treatment involve the use of agents that cause physical or chemical damage to the bacterium (3–10). For example, photodynamic therapy (PDT) uses light in the presence of a photosensitizer and oxygen to produce a highly reactive singlet of oxygen causing bacterial damage (8–10). The efficacy of PDT, however, is dependent on tissue oxidation, and bacterial infections in hypoxic environments, as seen in the late stages of osteomyelitis, may not be treatable with PDT (11,12).

Here we describe a new approach involving physical damage to the bacterium using a combination of pulsed laser energy and absorbing nanoparticles selectively attached to the bacterium. When nanoparticles are irradiated, they absorb energy, which is quickly transferred through nonradiative relaxation into heat and accompanied effects, and eventually leads to irreparable damage. Among the different nanostructures, gold nanoparticles, in different modifications (spherical, rods, shells, etc.), are the most promising candidates for such photothermal (PT) sensitizers because they are the strongest nanoabsorbers; their absorption coefficient due to profound plasmon resonance is at least if not more than three orders-of-magnitude greater when compared to other organic photosensitizers for PDT (13). Gold nanoparticles are photostable, nontoxic, and easily conjugated to antibodies (Abs) or proteins (13–19). In addition, their maximum absorption can be shifted to near-infrared spectral range (700–900 nm), allowing deeper penetration of the laser radiation into biotissues by the use of its shape and structure (e.g., shells or rods (13)), or by the self-assembly of the conventional spherical nanoparticles into nanoclusters (20,21).

To date, laser energy in combination with gold nanoparticles has been successfully used in killing cancer cells (17–21). In particular, selective PT tumor ablation has been demonstrated in animal models by exposing advanced nanoshells to long exposures (a few minutes) using a continuous-wave near-infrared laser (19). During long exposures, thermal diffusion distributes heat into the surrounding area, which effectively causes damage to a relatively large tumor mass. The pulse laser mode potentially provides more localized cellular damage, which might be important in killing individual metastatic or residual cells (17,18). Yet, without real-time dynamic monitoring of the laser-induced PT response, the local thermal effects may be insufficient to produce the desired therapeutic action, or, on the contrary, the strong PT and accompanied phenomena may counteract the precision of laser treatment and potentially damage surrounding healthy tissue. From this point of view, the PT techniques we describe here have shown the capability to detect single absorbing gold nanoparticles as small as 2-nm in size in vitro and in vivo (22–28) and time-resolved monitoring of the laser-induced microbubble dynamics around single and clustered nanoparticles during selective nanophotothermolysis (18,20,21). Because PT diagnostics and PT therapy are based on the phenomena of thermal origin, their integration into one multifunctional system allows us to realize selective nanophotothermolysis of cancer cells with real-time assessment of the efficiency of laser-induced bubble-formation phenomena leading to cancer cell death (20,21).

*Submitted March 1, 2005, and accepted for publication September 22, 2005.*
Address reprint requests to Vladimir P. Zharov, PhD, Tel.: 501-603-1213; Fax: 501-686-8029; E-mail: zharovvladimirp@uams.edu.

0006-3495/06/01/619/09 $2.00
doi: 10.1529/biophysj.105.061895

Here we adopt this principle to a new laser-nanoparticle-based PT antimicrobial therapy.

## MATERIALS AND METHODS

### Selective PT killing of *S. aureus* using gold nanoparticles

This concept assumes that one uses convectional (i.e., solid spheres), relatively small (e.g., 10–40 nm) gold nanoparticles that can be conjugated with specific Abs to selectively target the bacterium. These nanoparticles can attach to the bacterial surface individually or self-assemble under appropriate conditions into larger nanoclusters (Fig. 1 *a*). Gold nanoparticles strongly absorb laser irradiation; this absorbed energy transforms quickly into heat, which causes damage to the bacterium through local overheating effects and the accompanied bubble-formation phenomena. If many nanoparticles attach to the bacterial surface, there will be multiple damage sites with possible overlapping thermal spots from the particles within nanoclusters (Fig. 1 *b*). Nanocluster formation results in an enhancement of the PT killing effect because of 1), better heating efficiency resulting from an enhanced ability to confine the nanosecond laser-pulse within the nanocluster's size (21); 2), overlapping of bubbles from different nanoparticles within the nanoclusters decrease the bubble-formation threshold (20); and 3), an increase in the cluster's average local absorption and its potential red-shifting (from 525 nm for a single gold spherical nanoparticle to 700–800 nm for nanoclusters) in response to plasmon-plasmon resonance (20,21).

Monitoring the temperature in local heat zones around nanoparticles and the sizes of these zones are key issues in this approach. For the first approximation the maximum temperature around heated particles, $\Delta T_{max}$, in the absence of heat diffusion, can be estimated (29,30) as $\Delta T \cong \eta_T \alpha\Phi/\rho C$, where $\Phi$ is the incident laser fluence rate (J/cm$^2$), $\eta_T$ is the proportion of absorbed energy converted to heat (for gold $\eta_T \sim 1$ (31)), and $\alpha$, $\rho$, and $C$ are the particle coefficient absorption, density, and heat capacity, respectively. Assuming the Gaussian distribution of heat release $\Delta T\ (r,0) = \Delta T_{max} \exp(-r^2/R^2)$, the heat diffusion dynamic process after solving the standard diffusion equation can be described as (22,24)

$$\Delta T(r, t) = \Delta T_{max}(R_T^2/R^2)^{-3/2} \exp(-r^2/R_T^2), \quad (1a)$$

$$R_T(t) = (4kt + R^2)^{1/2}, \quad (1b)$$

where $R$ is the radius of the nanoparticle, and $R_T$ is the radius of the thermal spot on level $1/e$ for Gaussian temperature spatial distribution. Thus, heat diffusion leads to decrease temperature in the center as $\Delta T\ (0,t) = \Delta T\ (0, 0)_{max}\ [R/R_T\ (t)]^3$ and an increase in the thermal-spot size, $R_T$ (i.e., blurring effects) on the value $\Delta R = (4kt)^{1/2}$. The typical parameters used in this study were $\lambda = 0.5\ \mu$m: $NA = 0.4$, and $k = 1.44 \times 10^{-3}$ cm$^2$/s [water] (32). For short laser pulses $t_P$ (8 ns, as in the current experiment) and long continuous exposure (e.g., 2 min as in (19)), the $\Delta R$ parameter is ~69 nm and 9 mm, respectively. Long exposures might be useful for treatment of an extended infected area, but in a clinical setting, this mode may also damage surrounding healthy tissue. Short exposures have an advantage in that the heated volume and subsequent thermal damage, i.e., protein denaturation, coagulation, etc., is localized to the vicinity of the nanoparticles and their nanoclusters.

Using well-known theoretical models (17,22,29–32), we estimated that the maximum temperature around single 40-nm gold particles, at a laser fluence of 0.5 J/cm$^2$ after 8-ns laser pulse, is of the order of 1250°C, which is above a gold particles' melting point (1063°C), and in line with temperatures estimated by other researchers using similar conditions (17). This transient heat has the potential to cause physical damage to a staphylococcal cell wall with a typical thickness of 30- to 40-nm, through all of the following mechanisms: protein denaturation, melting of hot nanoparticles into the wall, and by sudden bubble formation around the nanoparticles. A consideration of nonlinear phenomena such as bubble formation has been the subject of many studies (e.g., (33,34)). In particular, temperature for nucleation is critical, and depends on many factors such as the rate of energy deposition, liquid parameters, and the size of the absorbing targets. Typically, the temperature ranges between 150 and 220°C with the bubble expanding and collapsing on the timescale of 0.1–5 $\mu$s. The pressure inside such a bubble is relatively high (up to $10^7$ Pa) (33) and can be accompanied by acoustic, mechanical, and chemical phenomena such as shock, acoustic waves, or the generation of radicals, which add to the stress on the cell wall.

### Targeting *S. aureus* with gold nanoparticles

The selective targeting of *S. aureus* was performed using a monoclonal antibody to one of the major surface-clustered proteins, protein A (*spa*), which is linked to the peptidoglycan portion of the cell wall (35,36) (Fig. 1 *a*). For these experiments, a staphylococcal clinical isolate, UAMS-1 (37,38,39), was cultured in tryptic soy broth and grown aerobically 16 h at 37°C. Cells were harvested by centrifugation, resuspended in sterile PBS to a concentration of $2 \times 10^8$ cells/ml, and incubated with a diluted (1:100) monoclonal anti-Protein A antibody (Sigma, St. Louis, MO) for 1.5 h at room temperature, rotating at low speed by a Roto-Shake Genie (Scientific Industries, Bohemia, NY). The bacteria were washed once with PBS for 5 min at 16,100 $\times$ *g* and then incubated with a secondary goat anti-mouse IgG (H+L) conjugated with 10-, 20-, or 40-nm gold particles (Ted Pella, Redding, CA) for 1 h at room temperature. For control purposes, UAMS-1 was incubated with unconjugated 10-, 20-, and 40-nm colloidal gold particles (Ted Pella) or with IgG conjugated gold particles without primary anti-Spa Abs. Specificity of the primary and secondary gold-conjugated Abs to protein-A was demonstrated by using Alexa Fluor 488-labeled chicken

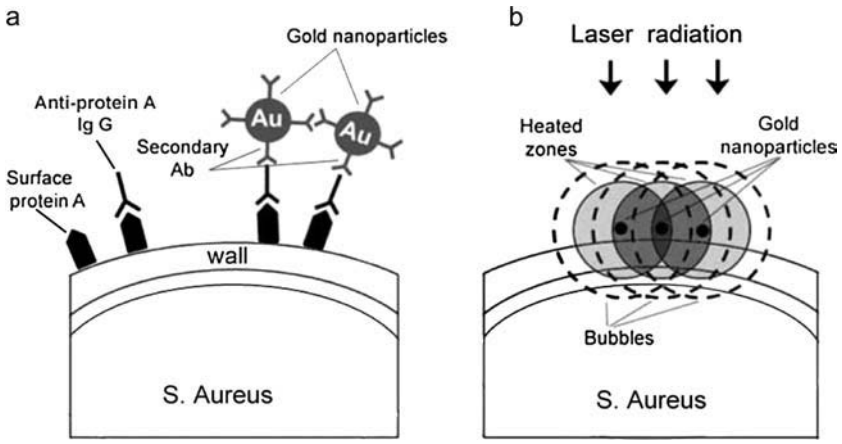


FIGURE 1 The principle of selective laser killing of *S. aureus* targeted with gold nanoparticles.

anti-mouse IgG and Alexa Fluor 594-labeled chicken anti-goat IgG antibodies (Molecular Probes, Eugene, OR).

## Laser treatment

*S. aureus* samples with or without gold nanoparticles were irradiated in an optical cuvette (Fisher Scientific, Pittsburg, PA) with quartz windows and a 2 × 20 × 10-mm dimension (light path of 10 mm, suspension height is 2 mm) using a Medlite IV Nd:YAG laser (Continuum Biomedical, Dublin, CA) in Q-switched mode with wavelengths of 532 nm and a 12-ns pulse width with a Gaussian intensity profile (2.5 mm at level *e*) formed with a long focus lens. Use of a 2-mm-square pinhole in front of the cuvette provided a relatively smooth beam-intensity profile and there was a relatively uniform irradiation of the entire sample in the cuvette at different fluences, 0.1–5 J/cm$^2$. After irradiation with 100 laser pulses, the samples were serial-diluted sixfold and plated on tryptic soy agar to quantify surviving colonies.

## Photothermal guiding of laser treatment

Because killing efficiency depends on local overheating effects accompanied by the bubble-formation phenomena, their formation was evaluated using PT technique, a method in which the general principle is based on similar phenomena (20–22,29,34). In these studies, we developed a new PT imaging (PTI) technique using a thermolens mode (27) on a technical platform of the Olympus BX51 microscope (Fig. 2) (Olympus, Melville, NY). Using the one-channeled thermolens mode, a single bacterium or several bacteria with or without attached nanoparticles were irradiated with a tunable optical parametric oscillator (spectral tuning range, 415–580 nm; pulse width, 8 ns; pulse energy, 0.1–300 $\mu$J, fluence 0.02–60 J/cm$^2$) from Lotis (Minsk, Belarus). Laser-induced local thermal and accompanied bubble-formation phenomena lead to temperature-dependent refractive index variations in the bacteria and in the medium surrounding the bacteria. These variations resulted in defocusing of the intensity which stabilized the continuous-wave He-Ne laser probe beam (wavelength, 633 nm; power, 1.4 mW, model 117A, Spectra-Physics, Mountain View, CA) by the so-called thermolens effect (29). The reduction of intensity at the center of the defocused probe beam was detected as integral PT response from whole bacteria by a photodiode (Model No. C5658; Hamamatsu, Shizuoka, Japan) with a 0.05-mm-diameter pinhole, and recorded with a TDS 3032B oscilloscope (Tektronix, Richardson, TX).

The second PTI mode (27) was based on irradiating bacteria with the pump laser pulse (the same as in the one-channeled thermolens mode), and detecting the defocusing effects of a second, co-linear laser probe pulse (Raman shifter, 639 nm; pulse width, 13 ns; pulse energy, 10 nJ) using a AE-260E CCD camera (512 × 512 pixels and pixel size of 20 $\mu$m (Apogee, Santa Monica, CA)). In this schematic, each pixel plays role of a single photodetector within a pinhole as in the one-channeled thermolens mode described above. Thus, a wide-field CCD-based PT microscope is equivalent to a multichanneled thermolens imaging system in which channel number is determined by number of pixels—521 × 512. This optical system satisfies the requirement for the creation of an adequate image because there is a correlation in the thermolens technique between optical fields immediately after the object is in the sample plane and the intensity distribution in the detected area (i.e., in the CCD pixel's plane) (29).

The entire imaging acquisition procedure in this mode included illumination of the bacteria with three pulses: an initial probe pulse followed by a 0.1-s delay to the pump pulse, and then a second probe pulse with a tunable delay (0–5000 ns) to the pump pulse. The calculation difference between the two probe images provided a PT image (30) that is dependent only on the coefficient absorption cross-section $\alpha$, which is transformed by the pump laser pulse through heating into a refractive index variation $\Delta n$ (i.e., $\alpha \rightarrow \Delta T \rightarrow \Delta n$), and excludes the possible influence of a phase distortion from the probe beam itself or from the natural refractive heterogeneities of bacteria. As a result, formation of a PT image required just one pump pulse with a relatively broad beam diameter. The time-consuming scanning with a strongly focused laser beam across the sample used in

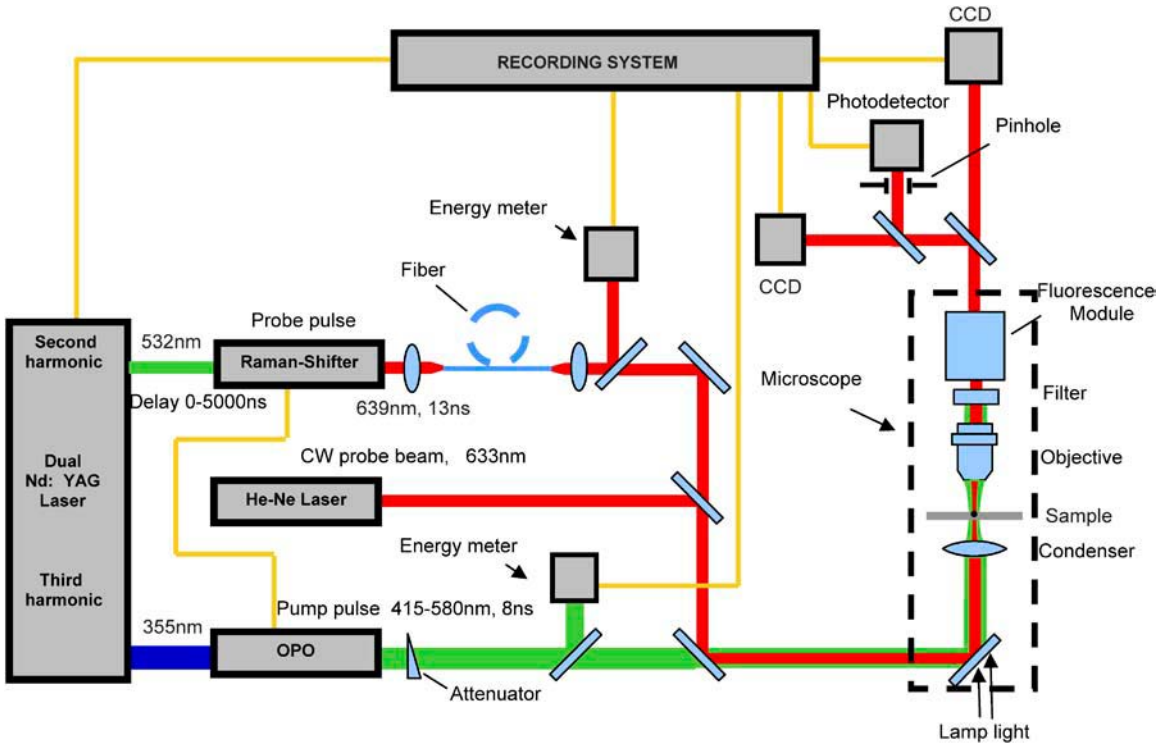


FIGURE 2 Schematics of integrated PT setup for diagnosis and therapy.

conventional confocal laser microscopy imaging is unnecessary. The chosen energy of the probe laser pulse (~10 nJ) was much lower than the pump-pulse energy permitted, thus minimizing the influence of probe-beam absorption by objects. The pump and probe beams had a stable, Gaussian intensity profile (controlled with the CCD camera), the diameters 23 $\mu$m and 17 $\mu$m, respectively, with laser fluence in the range of 0.02–60 J/cm$^2$. Pulse-to-pulse energy stability measured with an Ophir PE10/Nova-calibrated energy meter (Ophir Optronics, Danvers, MA) during 20 pulses was in the range of 3.8% for the whole pump beam and was ~6.5% for local points of the beam (i.e., hot spots) (22,34). Consequently, the possible influence of a nonsmooth intensity distribution in the cross-section of a laser beam, including hot spots, was reduced significantly. With the capture of each image, probe- and pump-pulse energy levels were measured simultaneously with photodiodes (Fig. 2), and the amplitude of each image pixel was normalized on laser pulse energy, which permitted the necessary compensation for possible variations in laser energy from pulse to pulse. The measurement of PT images at different time delays between pump and second probe pulses allowed time-resolved monitoring of the temporal dynamic of local thermal and accompanied bubble-formation effects.

Because of the laser beams' relatively broad sizes, conventional optical resolution $\delta_{OPT}$ was determined by diffraction-limited resolution of the microscope objective itself (e.g., ~0.7 $\mu$m at 20×, NA 0.4; and ~250 nm at 100×, NA 1.25). However, the resolution of PT microscope $\delta_{PT}$ is different from the conventional $\delta_{OPT}$ because it depends also on the factor $4kt$ (Eq. 1b), taking into account blurring of the diffraction spot due to heat diffusion during the laser pump pulse, i.e.,

$$\delta_{PT} = (\delta_{OPT}^2 + 4kt_P)^{1/2}. \quad (2)$$

For these experiments, $4kt_P \sim 69$ nm (see above), $\delta_{OPT} = 250$ nm, and we estimated $\delta_{PT}$ as 258 nm. Thus, the influence of heat diffusion on diffraction-limited resolution in current pulsed PTI is negligible ($\leq$3%).

## Transmission electron microscopy (TEM)

For obtaining transmission electron microscopy (TEM) images, bacteria samples were fixated in a composition of 2% paraformaldehyde and 2% glutaraldehyde in 0.12 M Sorensen's buffer at pH 7.4, then postfixated and stained in 2% osmium tetroxide solution for 1 h at 4°C. To eliminate any possibility of artifacts, the poststaining steps with uranyl acetate and lead citrate were omitted. After dehydration, embedding sections were cut on a MT6000 ultramicrotome (Sorvall, New Castle, DE). Thin sections (0.1 ÷ 0.05 $\mu$m) were examined and photographed using a JEOL 100CX electron microscope (JEOL-USA, Peabody, MA).

## Phase and fluorescence imaging

Phase contrast and transmittance images were processed at UAMS Deconvolution workstation via Axioskop 2 Mot Plus (Carl Zeiss, Jena, Germany) and digital camera Axio Cam MRm (Carl Zeiss) by using an oil immersion objective at magnification 100× and NA 1.3. Fluorescent images were recorded using systems of light filters for Texas Red (Chroma Technology, Rockingham, VT) or GFP (Omega Optical, Brattleboro, VT) dyes.

## RESULTS AND DISCUSSION

A comparison of conventional optical microscopy versus PT technique to visualize gold nanoparticles attached to the bacterium is demonstrated in Fig. 3. High-resolution phase contrast and transmission technique showed a very low image contrast to the bacteria alone and when associated with two 100-nm gold nanoparticles (Fig. 3 *a*), which is explained by the technique's low sensitivity (29). The sensitivity of PTI is at least four-orders-higher than the sensitivity of the transmission technique (30,34) and reveals some absorbing background that appears as a relatively large light spot on the PT image (Fig. 3 *b*). This absorption in the spectral range of 520–550 nm can be associated with cytochrome C found in *S. aureus* (35,36). The PT image of bacteria with 40-nm gold nanoparticles attached to the bacterial surface demonstrated a significant absorption contrast (Fig. 3 *c*) compared to the much lower PT image contrast from bacteria alone (Fig. 3 *b*). This contrast is explained by high absorption from gold nanoparticles due to plasmon resonance (13). The ability of PTI to visualize absorbing nanoscale particles with a far-field PT microscope is based on the imaging of a thermal spot around the nanoparticles in surrounding medium that expands resulting from heat diffusion (Eqs. 1a and 1b), and reaches the conventional diffraction limit of resolution (22,27). In the current experiments, the resolution for PTI mode $\delta_{PT}$ with a powerful micro-objective (100×, NA 1.25) was ~250 nm (see above). This is a significant improvement in resolution, which is 3–4 times greater when compared to previous data using PT phase contrast imaging (22,34). The brightness and size of the diffraction spot from several closely located nanoparticles, an average of 2–6, was greater than those of other spots containing a single nanoparticle; this finding was used to count the number of nanoparticles and nanoclusters per bacterium with a total of 30–40 optically disguisable nanoparticles. Comparison of the intensity of each spot at different time delays between pump and probe pulses, the PT

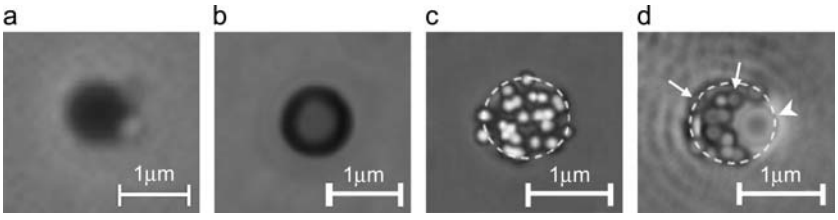


FIGURE 3 Images of *S. aureus* with attached gold nanoparticles: (*a*) phase contrast image (100×, NA 1.3); (*b*) PT image of bacteria alone (100×, NA 1.25, laser: 520 nm, 100 $\mu$J, with a fluence 20 J/cm$^2$); (*c*) PT images of bacteria with 40-nm gold particles at laser energy 2 $\mu$J (0.4 J/cm$^2$), time delay between pump and probe laser pulse 30 ns; and (*d*) PT images of bacteria with 40-nm gold particles at laser energy 10 $\mu$J (2 J/cm$^2$), time delay 120 ns. Dashed lines represent the bacterial boundary in *c* and *d*. Arrows in *d* indicate PT images of single nanoparticles, whereas the arrowhead shows a bubble around one nanocluster.

lifetime imaging mode (27), provided information on the dynamic of local thermal effects lasting 30–100 ns at a lower pulse energy level (<1 $\mu$J, fluence 0.2 J/cm$^2$) and 0.2–3 $\mu$s at a higher pulse energy level (>10 $\mu$J, 2 J/cm$^2$). Because thermal relaxation times $\tau_T$ for a spherical target with radius $R$, such that $\tau_T = R^2/6.75k$, where $k$ is thermal diffusivity (29), do not exceed 100 ns even for the largest nanoclusters (100–300 nm) (22), another mechanism, such as bubble formation, was involved in the formation of the PT images at high laser energy. In Fig. 3 *d*, the PT image at time-delay 120 ns, shows the initial temporal stage of one large bubble (indicated by *arrowhead*) developing around nanoclusters and was imaged because of the lower refractive index inside a bubble compared to surrounding liquid (34). At this time delay, the PT image contrast of single nanoparticles (indicated with *conventional arrows*) was much lower compared to a time delay of 30 ns (Fig. 3 *c*) due to fast cooling of the nanoparticles. These low-contrast images are likely associated with the pure thermal mechanism of PT response from single nanoparticles, because the efficiency generation of a bubble (with a longer lifespan) decreases with decreasing the particle sizes (17). PTI mode alone, however, does not permit the accurate monitoring of bubble-formation dynamics for the same bubble because to create several PT images several pump laser pulses are required that may destroy either the nanoparticles or bacterium, or at least modify their properties. To avoid this problem we applied a one-channeled thermolens mode to time-resolved monitoring integrated PT responses from a single bacterium with attached nanoparticles. At a moderate laser energy (~100 $\mu$J, 20 J/cm$^2$), the classic linear PT response (34) was observed for the control bacteria with no particles as indicated by an initial peak due to fast laser-induced heating of the bacteria, and a slower exponential tail corresponding to bacteria cooling as a whole through heat diffusion into the surrounding solution (Fig. 4 *a*). The minimum rise time of the PT response was determined by the laser pulse duration (8 ns) and the time response from the photodetector (10 ns). The cooling time for laser-heated bacteria ~400 ns was shorter than the cooling time of mammalian cells (20–40 $\mu$s) (34) due to the smaller bacterial size. Incubation of bacteria with gold nanoparticles led to dramatic increases in both linear and nonlinear phenomena. In particular, a stronger PT response from bacteria with attached nanoparticles was observed at lower laser energy (0.5 $\mu$J) as compared to bacteria alone (100 $\mu$J), and had a different shape (Fig. 4 *b*). The very narrow strong initial peak in the PT response is explained by very fast heating and cooling of strongly absorbing gold nanoparticles. Indeed, the thermal relaxation times $\tau_T$, of single nanoparticles or closely located or aggregated nanoparticles (nanoclusters) with sizes 40–400 nm in water-based solution, are 1–100 ns. The fast redistribution of heat from nanoparticles to the bacteria forms a secondary maximum in the PT response that has a slower rise and cooling time (Fig. 4 *b*).

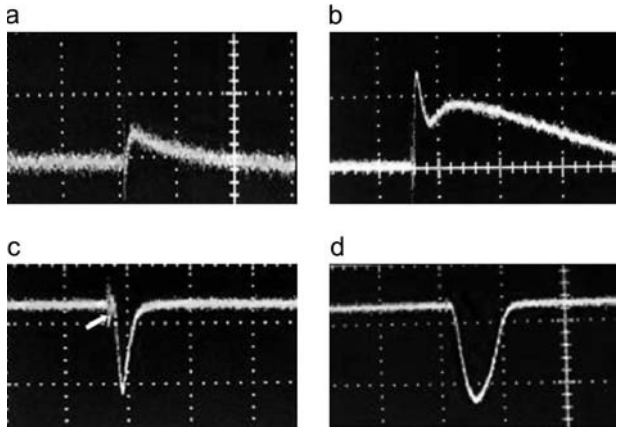


FIGURE 4 Integral PT responses from single *S. aureus* bacterium at a laser energy of 100 $\mu$J (*a*) and *S. aureus* with 40-nm gold nanoparticles at laser energies/fluence of 0.5 $\mu$J/0.1 J/cm$^2$ (*b*), 3.5 $\mu$J/0.7 J/cm$^2$ (*c*), and 10 $\mu$J/2 J/cm$^2$ (*d*). Amplitude (*vertical axis*)/timescale (*horizontal axis*) for images *a–d*: 50 mV/400 ns/div; 100 mV/100 ns/div; 200 mV/1 $\mu$s/div; and 500 mV/1 $\mu$s/div, respectively.

An increase in laser energy led to bubble formation around hot gold nanoparticles due to the overheating of the surrounding liquid layer. This phenomenon was indicated initially at the laser energy close to threshold bubble formation by the appearance of a small negative amplitude peak within a narrow positive signal (not shown). With further increases in the laser energy, a dramatic increase in the maximum amplitude of the negative peak occurred (Fig. 4, *c* and *d*); the increase was 1–2 orders-of-magnitude greater than that produced by bacteria without attached particles with another polarity (Fig. 4 *a*). The positive signals of pure thermal origin from nanoparticles (Fig. 4 *b*), which are smaller in amplitude and shorter in time compared to negative peaks associated with bubble formation, were hardly distinguishable in Fig. 4, *c* and *d*. These signals were also masked by the increased noise, like the fluctuation of PT response before bubble formation, which indicates a random nucleation dynamic with an average time of 10–50 ns (Fig. 4 *c*, *arrow*). A more detailed description of PT time-resolved monitoring of laser-induced bubble-formation phenomena around absorbing particles and their nanoclusters can be found in our recent publications (20–23,34). The formation of a negative peak can be explained by several effects such as the change in refractive index inside the bubble, scattering of light on the bubble, and a decrease in local temperature related to bubble-induced local cooling phenomena. After an initial expansion indicated by the rise-time of the negative peak, the vapor rapidly cools and condenses, and the bubbles collapse as indicated by the fall-time of the negative peak. The typical lifespan of the bubble ranges between 0.1 and 2 $\mu$s with a bubble size of 1–8 $\mu$m, respectively. These ranges are close to the Rayleigh relationship between bubble size and lifetime (33). The bubble sizes were roughly estimated by the comparison of PT bubble images at different time

delays between pump and probe laser pulses and bacteria size (Fig. 3 *d*). Thus, the characteristic temporal shape of the PT response and a dramatic increase in the PT response amplitude make it possible to identify bacteria labeled with nanoparticles in both linear and nonlinear PT thermolens modes. The integrated PT response and PT images from bacteria labeled with gold nanoparticles was easily detectable and repeatable even at a relatively low pulse energy level ($<1$ $\mu$J), although it disappeared with increased energy even after one or two laser pulses. This finding is related to thermal destruction of the particles by melting.

High temperatures and, especially, bubble-formation phenomena around attached nanoparticles caused physical damage to the bacterium as confirmed by TEM images (Fig. 5). At relatively low laser energies, we observed a very slight penetration of nanoparticles in the cell wall (Fig. 5 *b*, *arrows*) compared to the control without laser exposure (Fig. 5 *a*). Higher laser energies, or the formation of nanoclusters, led to a deeper penetration of nanoparticles inside the bacterial wall (Fig. 5 *c*, *arrows*). High laser energy and/or formation of nanoclusters coupled with multi-pulse exposure produced local cell-wall damage (Fig. 5 *d*, *arrow*) and finally complete bacterial disintegration (Fig. 5 *e*, shows fragmented bacteria), which can also be seen using optical imaging (Fig. 6). These data demonstrate that, despite the relatively high thickness and density of the bacterial cell wall, laser-induced thermal and bubble formation around nanoparticles may potentially cause irreparable damage to bacteria.

In previous experiments using laser energy and gold nanoparticles to kill cancer cells, we observed a maximal thermal effect with 30–40-nm size particles (18). In this work, we applied PT method to estimate efficiency of bubble formation for three particles sizes: 10-, 20-, and 40-nm. In analogy to the laser viability test (34), we measured the percentage of bacteria ($\eta$) with attached nanoparticles that produced a negative nonlinear PT response associated with the bubble formation when irradiated with one laser pulse (Fig. 4 *c*). This percentage was calculated as a ratio of $\eta = N_{neg}/N \times 100\%$, where $N$ is the total number of a single bacterium irradiated by one laser pulse of a 23-$\mu$m beam and $N_{neg}$ is the number of bacteria with a PT response containing a negative component. The irradiation of single bacterium was achieved by increasing the distance between bacteria through decreasing their concentration in solution. The

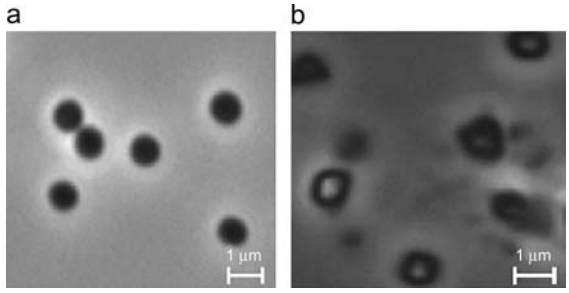


FIGURE 6 Phase-contrast images of *S. aureus* with 40-nm nanoparticles before (*a*) and after (*b*) laser exposure (532 nm; 12 ns; 3 J/cm$^2$, 100 pulses).

parameter $\eta$ is dependent on laser energy. With an increase in laser energy from 0.05 to 3$\mu$J, $\eta$ increases rapidly from 0% to 100%. At a fixed energy in the middle of this range, the parameter $\eta$ depends on the number of attached nanoparticles with the same size. On the other hand, at the same number of nanoparticles, this parameter will determine efficiency of bubble formation and hence, bacterial photodamage efficiency for nanoparticles with different sizes. For example, in Fig. 7, at a fixed energy and $\sim$30 attached nanoparticles, the maximum nonlinear PT response, which indicates the efficiency of bubble formation, was observed using 40-nm particles. Likewise in Fig. 8 *d*, efficient killing of *S. aureus* was achieved with 40-nm gold nanoparticles conjugated to a secondary IgG that targeted the bacterium by use of a primary protein A Abs. Control experiments with conventional optical imaging with fluorescent imaging using secondary Abs labeled with fluorescent marker revealed almost no direct binding of secondary Abs to bacterial surface in the absence of primary Abs (Fig. 8 *b*) compared to targeting the bacterium with primary Abs (Fig. 8 *c*). From these data, the specificity of targeting, defined as the ratio of the number of bacteria bound with gold nanoparticles at the double conjugations (i.e., with primary and secondary Abs) to the number of bacteria with nonspecific binding without primary Abs, was estimated as 98:1.

The ratio for binding to the bacteria compared to other cells (e.g., blood cells) is expected to be much higher, although this issue requires further investigation. In particular, protein A predominantly interacts with the Fc region of immunoglobulin G molecules (40–42). In our experiments, we did not observe significant killing using only gold nano-

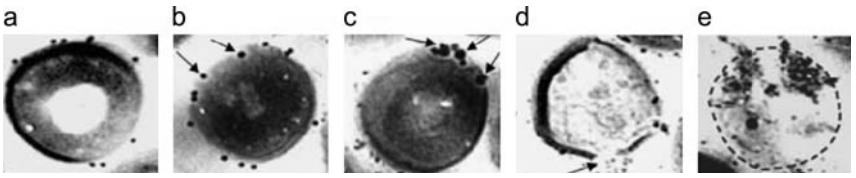


FIGURE 5 TEM images of *S. aureus* conjugated with gold nanoparticles before (*a*) and after (*b–e*) multilaser exposure of 100 pulses, wavelength of 532 nm, and pulse duration of 12 ns at a different conditions (see text): laser fluence of 0.5 J/cm$^2$ and no clusters (*b*); laser fluence of 0.5 J/cm$^2$ with clustered nanoparticles (*c*); and laser fluence of 3 J/cm$^2$ at one (*d*) and several (*e*) nanocluster numbers. A dashed line represents the bacterial boundary in *e*. Arrows in *b* and *c* indicate penetration of nanoparticles into the wall, and in *d*, arrows indicate local cell-wall damage.

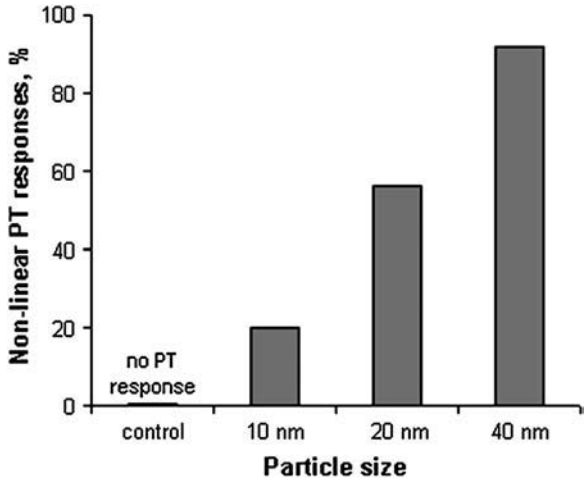


FIGURE 7 Nonlinear PT response from *S. aureus* as a function of nanoparticles size. Laser parameters: wavelength, 525 nm; pulse width, 8 ns; and pulse energy, 1 $\mu$J (0.2 J/cm$^2$).

particles conjugated with secondary Abs, which is explained by the proprietary methods used in manufacturing these molecules. The Fc region is linked directly to the gold colloid with the F(ab′)$_2$ regions remaining outside the Zeta Potential region of the colloid particles, and is free to interact with the primary protein-A Abs (personal communication, Dylan Herbert, British Biocell International, UK). Still, protein A can also interact with the F(ab′)$_2$-fragments of IgG, and may explain the slight increase in killing using the conjugated gold nanoparticles as compared with the colloid gold controls (42). Indeed, little effect was observed with unconjugated colloidal gold particles (Fig. 8 *d*). Direct irradiation of bacteria with laser did not damage them because of low absorption by natural endogenous cytochromes (35,36).

Using TEM and PTI, we estimated that the average number of attached nanoparticles was ~40–60 per bacterium. By TEM, this number was estimated from the perimeter of the fixed dead bacteria, the section thickness, and the number of particles observed. On the contrary, the advantage in using PTI was that we were able to calculate the total number of particles (if it is <50) with live bacteria in vitro, since this image is a two-dimensional projection of three-dimensional bacterial volume. This relatively small amount was chosen as an approximation to practical condition. According to obtained data at a higher laser energy level (fluence, 3–5 J/cm$^2$), 1–3 laser pulses was sufficient to damage bacteria, whereas at a lower fluence (~0.5–1 J/cm$^2$), at least 100 pulses is required to produce the harmful effects on bacteria (Fig. 9). However, maximum number of binding gold particles to *S. aureus* may be significantly higher (e.g., 2300 for 20-nm particles) (43). Because the efficiency of killing is directly related to the number of particles, the presented technology has tremendous potential for further development in reducing the laser fluence levels to 100 mJ/cm$^2$, which is established as the safety standard for medical lasers (44).

## CONCLUSION

By combining the three approaches, nanoparticles, laser, and PT technique, we have successfully achieved localized killing of *S. aureus* in vitro. We have demonstrated that PT technique using a new PT thermolens imaging mode and conjugated gold nanoparticles, especially nanocluster formation, may be used to optimize the efficiency of laser-induced bacterial cell killing by 1), providing temporal and spatial confinements of the laser parameters with the use of

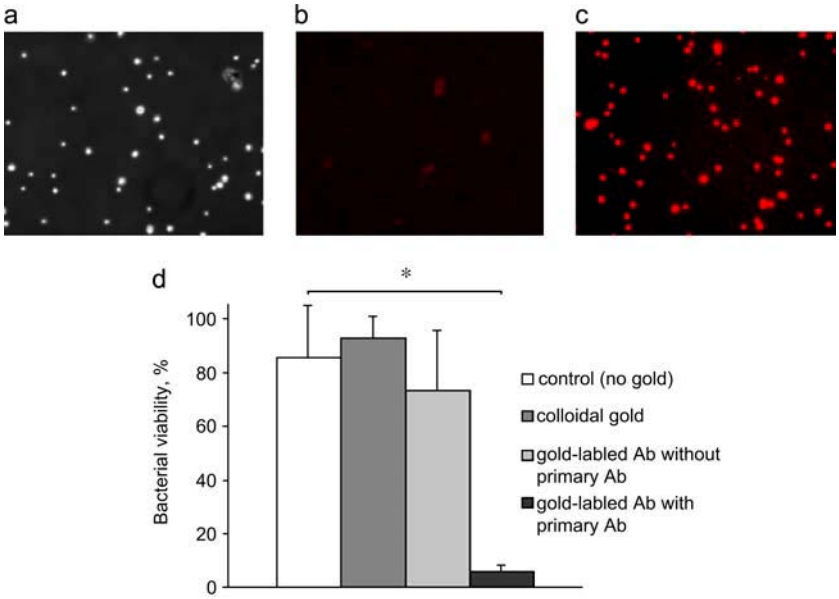


FIGURE 8 Selectivity of binding *S. aureus* with bioconjugated gold nanoparticles. The phase contrast (*a*) and fluorescent images of *S. aureus* labeled with chicken anti-goat IgG as secondary antibodies with Alexa Fluor 594 without (*b*) and with (*c*) the primary chicken-anti-mouse IgG antibody labeled with Alexa Fluor 488. Bacterial viability was assessed after laser exposure (532 nm, 12 ns, 3 J/cm$^2$) using 40-nm gold nanoparticles by plating the sample on tryptic soy agar (*d*). The results of plate counting of samples without laser treatment were assumed as 100%. Statistical values were reported as means ± SD of two independent experiments in triplicates. Differences between means were calculated by Student's *t*-test for paired values. (*$p = 0.0006$.)

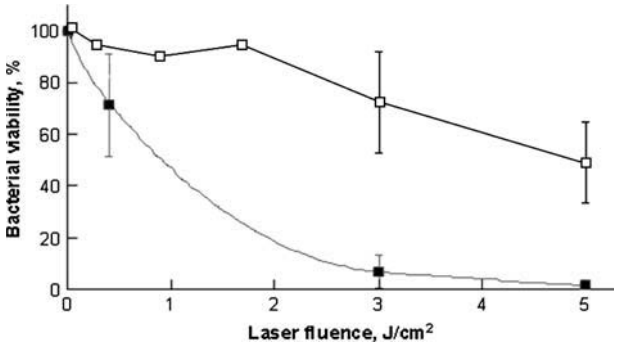


FIGURE 9 Efficiency of laser killing of *S. aureus* targeted with 40-nm gold nanoparticles as a function of laser fluence (0–5 J/cm$^2$). Bacterial viability was assessed by plate counting. Laser parameters are: wavelength, 532 nm; pulse width, 12 ns; and number of pulses, 100. The open squares represent samples irradiated without gold nanoparticles; the solid squares represent samples irradiated with attached gold nanoparticles. The plate-counts of samples without laser treatment were assumed 100% viable. Statistical values are reported as means ± SD of three independent experiments in duplicates.

different types and sizes of nanoparticles; 2), high resolution (250 nm) visualization of the spatial location of a single nanoparticle attached to a bacterium; and 3), the study of the mechanism and threshold of bacterial damage. Thus, PTI and integrated PT response modes supplement each other and, in combination, provide spatial localization and monitoring of bubble-formation dynamics surrounding single nanoparticles and their nanoclusters attached to the bacterial wall. The correlation observed between a bubble formation and bacterial damage permits using PT technique to estimate rapidly the noninvasive and invasive conditions of the impact of laser energy on single bacterium. This technique has also shown the capability to control in real-time the efficiency of attaching conjugated nanoparticles to the bacterial surface as well as calculate the total number of attached particles to one bacterium at different conditions.

In general, our research is a preliminary step toward developing integrated nanomedicine, which combines nanotherapeutics with simultaneous nanodiagnostics for guiding, and optimization of thermal-based laser treatment. PT technique is a powerful tool that can monitor thermal and accompanied effects at broad temperature ranges from a few degrees (diagnostics) to several hundred or thousand degrees (therapeutics). We believe this approach may be applicable as a therapeutic strategy for infections caused by other types of bacteria, and potentially viral infections (e.g., hepatitis), since both can be labeled with gold nanoparticles (23,45). Furthermore, we plan to transit this technology to an in vivo animal study, using the principle of integrated PT flow image cytometry, which has been used to detect gold nanoparticles in bioflow in vivo (28), or in combination with fluorescence and photoacoustic technique (22) to monitor transportation particles in blood and lymph flow and their accumulation in specific sites.

The authors thank Dr. T. Sims (Department of Neurobiology and Developmental Biology, University of Arkansas for Medical Sciences) for his assistance with the TEM technique, Ekaterina Galanzha, PhD, for her assistance with statistical data, and Scott Ferguson for his assistance with laser measurements.

This work was supported by the Department of Defense (grant No. DAMD17-03-1-0579), in part by the National Science Foundation (grant No. BES 0119470), and by the National Institutes of Health/National Institute of Biomedical Imaging and Bioengineering (grant No. R01 EB000873). (V. Zharov was the Principle Investigator in all grants.)

## REFERENCES

1. Chopra, I. 2003. Antibiotic resistance in *Staphylococcus aureus*: concerns, causes and cures. *Expert Rev. Anti Infect. Ther.* 1:45–55.
2. Gemmell, G. C. 2004. Glycopeptide resistance in *Staphylococcus aureus*: is it a real threat? *J. Infect. Chemother.* 10:69–75.
3. Novick, R. P. 2003. Autoinduction and signal transduction in the regulation of staphylococcal virulence. *Mol. Microbiol.* 48:1429–1449.
4. Cheung, A. L., A. S. Bayer, G. Zhang, H. Gresham, and Y. Q. Xiong. 2004. Regulation of virulence determinants in vitro and in vivo in *Staphylococcus aureus*. *FEMS Immunol. Med. Microsc.* 40:1–9.
5. Moritz, A., O. Doertbudak, N. Gutknecht, K. Goharkhay, U. Schoop, and W. Sperr. 1997. Nd:YAG laser irradiation of infected root canals in combination with microbiological examinations. *J. Am. Dent. Assoc.* 128:1525–1530.
6. Rojo, A., E. Ferrer, C. Torron, M. C. Villuendas, O. Ruiz, L. Pablo, and F. M. Honrubia. 2000. Nd-YAG capsulotomy and intravitreal antibiotics as treatment of chronic endophthalmitis. *Arch. Soc. Esp. Oftalmol.* 75:109–116.
7. Ellis, S. L., P. Finn, M. Noone, and D. J. Leaper. 2003. Eradication of methicillin-resistant *Staphylococcus aureus* from pressure sores using warming therapy. *Surg. Infect. (Larchmt).* 4:53–55.
8. Gad, F., T. Zahra, K. P. Francis, T. Hasan, and M. R. Hamblin. 2004. Targeted photodynamic therapy of established soft-tissue infections in mice. *Photochem. Photobiol. Sci.* 3:451–458.
9. Embleton, M. L., S. P. Nair, B. D. Cookson, and M. Wilson. 2002. Selective lethal photosensitization of methicillin-resistant *Staphylococcus aureus* using an IgG-tin (IV) chlorin e6 conjugate. *J. Antimicrob. Chemother.* 50:857–864.
10. Embleton, M. L., S. P. Nair, B. D. Cookson, and M. Wilson. 2004. Antibody-directed photodynamic therapy of methicillin resistant *Staphylococcus aureus*. *Microb. Drug Resist.* 10:92–97.
11. Fuchs, J., and J. Thiele. 1998. The role of oxygen in cutaneous photodynamic therapy. *Free Radic. Biol. Med.* 24:835–847.
12. Calhoun, J. H., J. A. Cobos, and J. T. Mader. 1991. Does hyperbaric oxygen have a place in the treatment of osteomyelitis? *Orthoped. Clin. NA.* 22:467–471.
13. West, J. L., and N. J. Halas. 2000. Applications of nanotechnology to biotechnology commentary. *Curr. Opin. Biotechnol.* 11:215–217.
14. Jain, K. K. 2003. Nanodiagnostics: application of nanotechnology in molecular diagnostics. *Expert. Rev. Mol. Diag.* 3:153–161.
15. Daniel, M. C., and D. Astruc. 2004. Gold nanoparticles: assembly, supramolecular chemistry, quantum-size-related properties, and applications toward biology, catalysis, and nanotechnology. *Chem. Rev.* 104:293–346.
16. Brigger, I., C. Dubernet, and P. Couvreur. 2002. Nanoparticles in cancer therapy and diagnosis. *Adv. Drug Deliv. Rev.* 54:631–651.
17. Pitsillides, C. M., E. K. Joe, X. Wei, R. R. Anderson, and C. P. Lin. 2003. Selective cell targeting with light-absorbing microparticles and nanoparticles. *Biophys. J.* 84:4023–4032.
18. Zharov, V., V. Galitovsky, and M. Viegas. 2003. Photothermal detection of local thermal effects during selective nanophotothermolysis. *Appl. Phys. Lett.* 83:4897–4899.

19. O'Neal, D. P., L. R. Hirsch, N. J. Halas, J. D. Payne, and J. L. West. 2004. Photo-thermal tumor ablation in mice using near infrared-absorbing nanoparticles. *Cancer Lett.* 209:171–176.

20. Zharov, V. P., R. R. Letfullin, and E. N. Galitovskaya. 2005. Microbubbles-overlapping mode for laser killing of cancer cells with absorbing nanoparticle clusters. *J. Phys. D: Appl. Phys.* 38:2571–2581.

21. Zharov, V. P., E. N. Galitovskaya, C. Jonson, and K. Thomas. 2005. Synergistic enhancement of selective nanophotothermolysis with gold nanoclusters: potential for cancer therapy. *Laser Surg. Med.* 37:219–226.

22. Zharov, V. P., and D. O. Lapotko. 2005. Photothermal imaging of nanoparticles and cells. *IEEE J. Sel. Topics Quant. Electrons.* 11:In Press.

23. Zharov, V. P., J.-W. Kim, M. Everts, and D. T. Curiel. 2005. Self-assembling nanoclusters in living systems: application for integrated photothermal nanodiagnostics and therapy. *J. Nanomed.* 12:In Press.

24. Lapotko, D. O., T. R. Romanovskaya, A. Shnip, and V. P. Zharov. 2002. Photothermal time-resolved imaging of living cells. *Lasers Surg. Med.* 31:53–63.

25. Zharov, V. P., and D. O. Lapotko. 2003. Photothermal sensing of nanoscale targets. *Rev. Sci. Instrum.* 74:785–788.

26. Cognet, L., C. Tardin, D. Boyer, D. Choquet, P. Tamarat, and B. Lounis. 2003. Single metallic nanoparticle imaging for protein detection in cells. *Proc. Natl. Acad. Sci. USA.* 100:11350–11355.

27. Zharov, V. 2003. Far-field photothermal microscopy beyond the diffraction limit. *Opt. Lett.* 28:1314–1316.

28. Zharov, V. P., E. I. Galanzha, and V. V. Tuchin. 2005. Photothermal image flow cytometry *in vivo*. *Opt. Lett.* 30:628–630.

29. Zharov, V. P., and V. S. Letokhov. 1986. Laser Optoacoustic Spectroscopy. Springer-Verlag, Berlin, Heidelberg, and New York.

30. Lapotko, D., T. Romanovskaya, and V. Zharov. 2002. Photothermal images of live cells in presence of drug. *J. Biomed. Opt.* 7:425–434.

31. Huttmann, G., and R. Birngruber. 1999. On the possibility of high-precision photothermal microeffects and the measurement of fast thermal denaturation of proteins. *IEEE J. Sel. Topics Quant. Electrons.* 5:954–962.

32. Letokhov, V. S. 1991. Effects of transient local heating of spatially and spectrally heterogeneous biotissue by short laser pulses. *Nuovo Cimento.* D13:939–948.

33. Venugopalan, V., A. Guerra 3rd, K. Nahen, and A. Vogel. 2002. Role of laser-induced plasma formation in pulsed cellular microsurgery and micromanipulation. *Phys. Rev. Lett.* 88:078103.

34. Lapotko, D. O., and V. P. Zharov. 2005. Spectral evaluation of laser-induced cell damage with photothermal microscopy. *Laser Surg. Med.* 36:22–30.

35. Navarre, W. W., and O. Schneewind. 1999. Surface proteins of Gram-positive bacteria and mechanisms of their targeting to the cell wall envelope. *Microbiol. Mol. Biol. Rev.* 63:174–229.

36. Forsgren, A., V. Ghetie, R. Lindmark, and J. Sjöquist. 1983. Protein A and its exploitation. *In Staphylococci* and Staphylococcal Infection. C.S.F. Easmon, and C. Adlam, editors. Academic Press, London. 429–480.

37. Gillaspy, A. F., S. G. Hickmon, R. A. Skinner, J. R. Thomas, C. L. Nelson, and M. S. Smeltzer. 1995. Role of the accessory gene regulator (AGR) in pathogenesis of staphylococcal osteomyelitis. *Infect. Immun.* 63:3373–3380.

38. Smeltzer, M. S., J. R. Thomas, S. G. Hickmon, R. A. Skinner, C. L. Nelson, D. Griffith, T. R. Parr, Jr., and R. P. Evans. 1997. Characterization of a rabbit model of staphylococcal osteomyelitis. *J. Orthop. Res.* 15:414–421.

39. Blevins, J. S., M. O. Elasri, S. D. Allmendinger, K. E. Beenken, R. A. Skinner, J. R. Thomas, and M. S. Smeltzer. 2003. Role of sarA in the pathogenesis of *Staphylococcus aureus* musculoskeletal infection. *Infect. Immun.* 71:516–523.

40. Lindmark, R., K. Thoren-Tolling, and J. Sjoquist. 1983. Binding of immunoglobulins to protein A and immunoglobulin levels in mammalian sera. *J. Immunol. Methods.* 62:1–13.

41. Bacigalupo, M. A., C. Iacobello, G. Meroni, and A. Ius. 1992. Affinity of Europium-labelled proteins A and G for immunoglobulin G from seven mammalian species. *Eur. J. Clin. Chem. Clin. Biochem.* 30: 529–530.

42. Ljungberg, U. K., B. Jansson, U. Niss, R. Nilsson, B. E. Sandberg, and B. Nilsson. 1993. The interaction between different domains of staphylococcal protein A and human polyclonal IgG, IgA, IgM and F(ab′)2: separation of affinity from specificity. *Mol. Immunol.* 30: 1279–1285.

43. Kehle, T., and V. Herzog. 1987. Interactions between protein-gold complexes and cell surfaces: a method for precise quantitation. *Eur. J. Cell Biol.* 45:80–87.

44. American National Standard for Safe Use of Lasers. 2000. *ANSI* Z136.1.

45. Dragnea, B., C. Chen, E. S. Kwak, B. Stein, and C. C. Kao. 2003. Gold nanoparticles as spectroscopic enhancers for in vitro studies on single viruses. *J. Am. Chem. Soc.* 125:6374–6375.